Phase selective synthesis of nickel silicide nanocrystals in molten salts for electrocatalysis of the oxygen evolution reaction

Ram Kumar, Mounib Bahri, Yang Song, Francisco Gonell, Cyril Thomas, Ovidiu Ersen, Clément Sanchez, Christel Laberty-Robert, David Portehault

Phase selective synthesis of nickel silicide nanocrystals in molten salts for electrocatalysis of the oxygen evolution reaction

Ram Kumar,[a] Mounib Bahri,[b] Yang Song,[a] Francisco Gonell,[a] Cyril Thomas,[c] Ovidiu Ersen,[b] Clément Sanchez,[a] Christel Laberty-Robert,[a] David Portehault[a,*]

.

We report phase selective synthesis of intermetallic nickel silicide nanocrystals in inorganic molten salts. NiSi and Ni2Si nanocrystals are obtained by reacting a nickel (II) salt and sodium silicide Na_4Si_4 in the molten LiI-KI inorganic eutectic salt mixture. We report that nickel silicide nanocrystals are precursors to active electrocatalysts in the oxygen evolution reaction (OER) and may be low-cost alternatives to iridium-based electrocatalysts.

Introduction

Transition metal silicides are an important class of refractory intermetallics with high thermal, chemical and mechanical stabilities.[1,2] Depending on their constituent metals and stoichiometry, metal silicides can exhibit a range of crystal structures, electronic, magnetic and catalytic properties.[3–5] For example, the six stable bulk phases of nickel silicides Ni_3Si, Ni_2Si, $Ni_{31}Si_{12}$, Ni_3Si_2, NiSi and $NiSi_2$ show close stoichiometry but significantly different structures and functional properties. The investigation of their structure-property relationships has resulted in silicide materials performing in electronics,[6] thermoelectricity[7] and catalysis.[8] These properties are generally strongly influenced or improved (e.g. in catalysis) at the nanoscale. However, conventional synthesis of silicides involves high temperatures and long duration solid-state techniques using bulk elements as starting precursors.[9] Hence, the usual solid-state chemistry routes[1] are not suitable to produce nanoscaled metal silicides. Some efforts have been devoted to synthesize metal silicides at the nanoscale using chemical vapour deposition[10,11] and very few reports have dealt with colloidal synthesis in organic solvents[12,13] or molten salt-assisted magnesiothermic reduction.[14] Up to now, the latter techniques have resulted in low yield and a poor control over composition and phase purity. Synthesis in organic solvents result in materials surfaces covered with organic ligands, often strongly altering any catalytic activity and investigation of charge transport properties. The study of nanostructures of metal silicides then faces a synthetic bottleneck.

We identified two major constraints in the currently available colloidal syntheses of silicides: (i) the available Si sources SiH_4 and silanes are difficult to handle and often result in poor stoichiometry control;[11,12] and (ii) the required temperatures to obtain various silicide phases are too high to be compatible with common organic solvents and ionic liquids.[1] Indeed, organic liquid-phase synthesis above ca. 200 °C may result in side reactions forming eg. metal carbides as side products or surface species difficult to detect.[15,16] In the present work we addressed both of these aspects (**Scheme 1**) by employing (i) the reactive ionic Zintl solid Na_4Si_4 as Si source[17] and (ii) a carbon-free inorganic

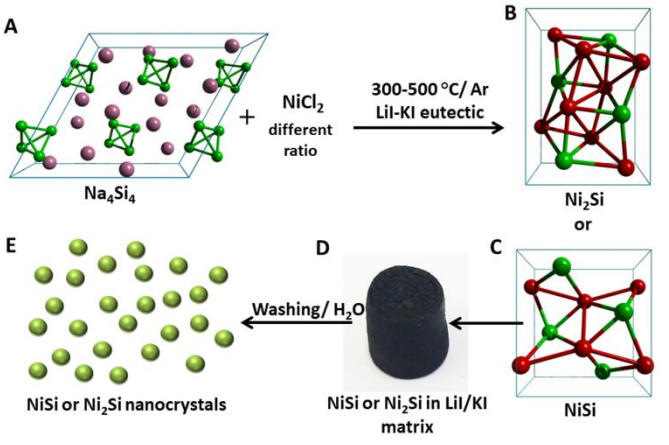

Scheme 1 (A) Reaction of the ionic Zintl solid Na_4Si_4 with different ratios of $NiCl_2$ in molten LiI-KI eutectic mixture (pink spheres = Na^+, green tetrahedra = $[Si_4]^{4-}$). (B, C) Phase selective synthesis of NiSi and Ni_2Si (red sphere = Ni, green sphere = Si). (D, E) NiSi or Ni_2Si embedded in LiI-KI matrix after reaction, and subsequent washing in acidic water to obtain the nanocrystals.

molten salt as a high temperature solvent.[18] We used the molten LiI-KI eutectic mixture (LiI:KI = 63:37 mol. ratio, m.p. = 286 °C). Its viscosity comparable to water, it's wide thermal stability window and its negligible vapour pressure at ~500 °C provide access to versatile temperature and composition conditions. Liquid media enhance atom diffusion and thus increase reaction rates and lower reaction temperatures compared to solid-state processes. Out of the six stable bulk nickel silicide phases mentioned above,[1] Ni_2Si and NiSi (**Scheme 1**) enable to validate our synthesis strategy.

Nickel borides[19] and nickel phosphides[20,21] have raised considerable interest during the last years as precursors to low-cost earth abundant electrocatalysts. These materials may be alternatives to precious metal-based electrocatalysts of the oxygen evolution reaction (OER) in alkaline water electrolyzers.[22,23] As another family of nickel-p-block element compounds, nickel silicides nanocrystals appear as potential candidates for OER electrocatalysis, although they have not been reported as such to date. More generally, metal silicides are largely underexplored as precursors to alternative OER electrocatalysts due to the synthesis bottlenecks detailed above.[24] Synthesis in molten salts may yield nanocrystals with high surface area and with surfaces free of any insulating organic ligands, hence particularly suitable for charge transfer and then electrocatalysis. The present work is the first report on the use of nickel silicide nanocrystals in OER electrocatalysis.

Results and discussion

Scheme 1 shows the synthesis process. The Na_4Si_4 precursor comprises covalently bonded $[Si_4]^{4-}$ tetrahedra[25] with Si(-I) species acting both as silicon source and reducing agent to react with a Ni(II) salt. We reacted different ratios of Na_4Si_4 and $NiCl_2$ at 300-500 °C in the LiI-KI eutectic mixture to obtain Ni_2Si and NiSi nanocrystals, respectively. By using this molten salt synthesis approach, we gained significant control over the phase purity (see ESI for details of the synthesis conditions). **Figure S1** (ESI) shows the powder X-ray diffraction patterns of the NiSi and Ni_2Si products. NiSi crystallizes in the orthorhombic space group P*nma* (62).[26] Ni_2Si is obtained predominantly as the orthorhombic P*bnm* (62) polymorph with a low amount of the hexagonal P*63/mmc* (194) phase.[27] All these structures consist in Ni–Ni and Ni–Si bonds. NiSi and Ni_2Si are reported to exhibit a metallic behaviour.[28]

Transmission electron microscopy (TEM, **Figures 1** and **S2**) images indicate that Ni_2Si is obtained as nanocrystals. The size distribution (**Figure S3**) shows a diameter between 7-16 nm

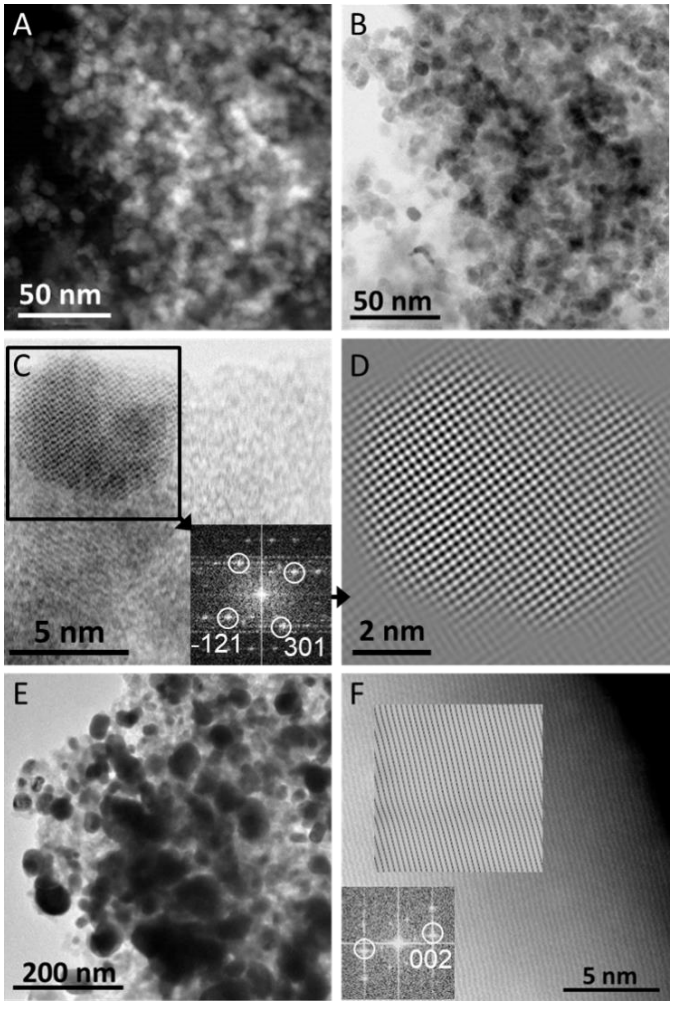

Fig. 1 (A, B) High-angle annular dark-field (HAADF) and bright field (BF)-scanning transmission electron microscopy (STEM) images of Ni_2Si nanocrystals. (C) STEM image of o-Ni_2Si nanocrystals with a Fast Fourier Transform (FFT) indexed along the o-Ni_2Si structure and showing the spots used to yield the FFT-filtered image of the o-Ni_2Si nanocrystal in (D). (E) TEM and (F) HAADF-STEM images of NiSi nanocrystals. The corresponding FFT indexed along the NiSi structure shows spots used to yield the inserted FFT-filtered image.

Ni_2Si nanocrystals. Selected area electron diffraction (SAED) (**Figure S2**), high resolution TEM (HRTEM) and scanning STEM images (**Figure 1C, D**) confirm the crystal structure of Ni_2Si (**Figures 1C**,**D** and **S2**). The uniform contrast observed by high angle annular dark field-STEM (STEM-HAADF, **Figure 1A**) and the uniform distribution of Ni and Si highlighted by STEM coupled to energy dispersive X-ray spectroscopy (STEM-EDX, **Figure S4**) confirm the compositional homogeneity of the Ni_2Si nanocrystals. TEM images of NiSi nanocrystals are shown in **Figures 1E** and **S5**. Well-faceted 15-45 nm NiSi nanocrystals with an average particle size of ca. 30 nm (**Figure S6**) are observed. STEM-HAADF (**Figure 1F**) shows lattice fringes confirming the crystal structure and high crystallinity of the NiSi nanocrystals. Elemental STEM-EDX mapping provides further support to the compositional homogeneity of NiSi nanocrystals (**Figure 2**).

The Hume-Rothery rule[29] states that one factor governing the formation of intermetallic compounds through the lattice

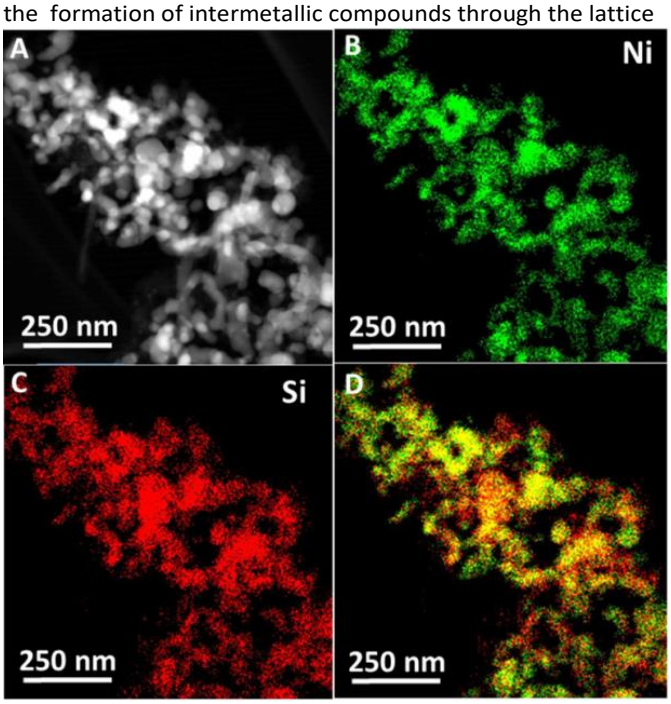

Fig. 2 (A) STEM-HAADF image and corresponding STEM-EDX mapping of NiSi nanocrystals. (B) Nickel (green), (C) silicon (red) and (D) combined Ni and Si maps.

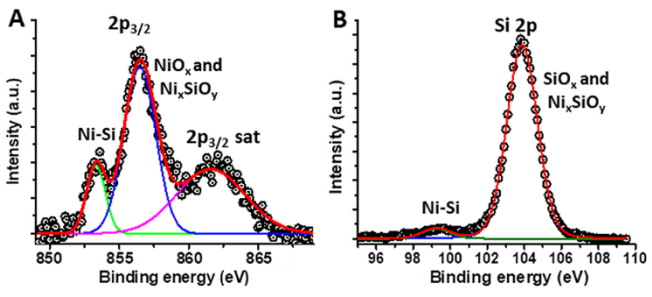

Fig. 3 (A) Ni $2p_{3/2}$ and (B) Si 2p core level regions of XP spectra of NiSi nanocrystals.

energy gain is the electronegativity difference and the charge transfer between the different constituent atoms. This is reflected in the X-ray photoelectron spectra (XPS) of NiSi (**Figures 3**, **S7** and **Table S1**) and Ni_2Si (**Figure S8** and **Table S2**).

The Ni $2p_{3/2}$ binding energy for NiSi and Ni_2Si is 853.3 and 853.1 eV, respectively. These values are higher than those observed for metallic Ni(0) at around 852.3 eV,[30] and smaller than the values for Ni(II) species observed at around 856 eV (**Tables S1** and **S2**). These observations are consistent with partial charge transfer from Ni to Si[31] in the silicide nanocrystals. Likewise, the Si 2p binding energy of 99.2 eV can be attributed to the intermetallic Ni_xSi compounds.[31] NiO_x and Ni_xSiO_y species are also detected in the Ni $2p_{3/2}$ region at 856.5 and 856.2 eV for NiSi and Ni_2Si, respectively. Oxidized silicon species[32] are also observed at Si 2p binding energies of 103.8 and 103.7 eV for NiSi and Ni_2Si, respectively. Oxidized Ni and Si species originate from an oxidized layer formed during washing of the samples with water and further exposure to air.[33,34] Nonetheless, the nanocrystals are remarkably stable in contact with an alkaline aqueous medium, as shown by the absence of modification of the XRD pattern of Ni_2Si after exposure to a 2 mol L^{-1} aqueous NaOH solution (**Figures S9, S10**).

Nitrogen sorption isotherms of NiSi and Ni_2Si (**Figure S11**) show a type–II profile representative of non-porous solids.[35] The Brunauer-Emmett-Teller (BET) specific surface area was evaluated at 24 and 18 $m^2\ g^{-1}$ for NiSi and Ni_2Si, respectively. The relatively high specific surface area for such compounds, their chemical stability and the absence of insulating organic surface ligands motivated us to explore the properties of nickel silicide nanocrystals as potential earth abundant intermetallic electrocatalysts. We have assessed the electrocatalytic properties for the oxygen evolution reaction (OER) in a basic electrolyte (0.1 M KOH, see ESI).

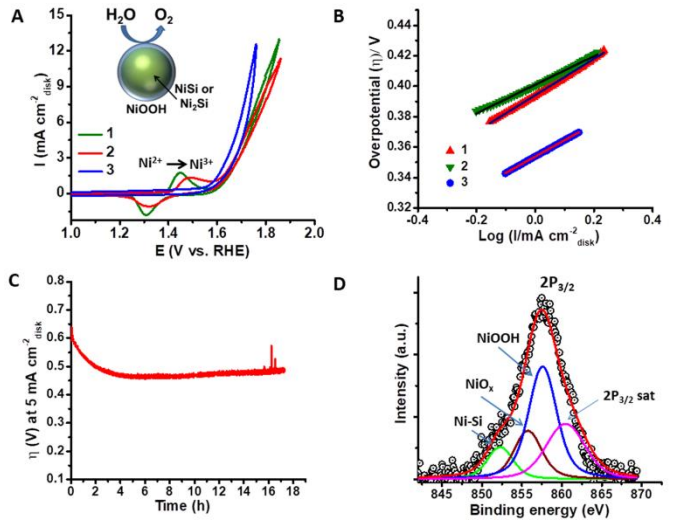

Fig. 4 (A) Cyclic voltammograms of (1) Ni_2Si, (2) NiSi and (3) commercial reference IrO_2 in O_2-saturated 0.1 M KOH at a scan rate of 10 mV s^{-1} and a constant electrode rotation of 1600 rpm. (B) Tafel plots of (1) NiSi, (2) Ni_2Si and (3) IrO_2. (C) Chronopotentiometry stability test of NiSi at a constant current density of 5 mA cm^{-2}_{disk} and electrode rotation of 1600 rpm. For all curves, the potential was corrected for the iR_s drop. (D) Ni $2p_{3/2}$ XPS spectrum of NiSi electrode after galvanostatic stability test.

The materials were drop-casted on glassy carbon substrates from conductive inks comprising carbon black, Nafion®, and the electrocatalyst nanocrystals. **Figure 4A** shows cyclic voltammograms (CVs) recorded on rotating working electrodes for NiSi, Ni_2Si and reference commercial IrO_2 after correction for the resistance of the electrolyte (iR_s corrected potential) with R_s the uncompensated ohmic resistance from the electrolyte. A current density of 10 mA cm^{-2}_{disk} was achieved at an overpotential of ca. 0.57 V/RHE for NiSi and Ni_2Si, whereas we measured an overpotential of c.a. 0.50 V/RHE for commercial reference IrO_2.

The Tafel slopes for NiSi, Ni_2Si and IrO_2 is 119, 94 and 107 mV dec^{-1}, respectively (**Figure 4B**). The reversible anodic peak at about 1.4 V/RHE (**Figure 4A**) is in agreement with an oxidation of Ni^{2+} species to Ni^{3+}.[36] Therefore, the native oxidized surface Ni^{2+} species are reversibly oxidized, most probably into a phase related to NiOOH, which is electrocatalytically active in OER.[36,37,38] Thus nickel silicide nanocrystals in alkaline OER conditions undergo surface modification and formation of an electrocatalytically active NiOOH shell with a metallic NiSi or Ni_2Si core (inset **Fig. 4A**).[19] We hypothesize that the conducting metallic core promotes the formation of electrochemically active NiOOH shell while maintaining large charge percolation favourable to electrocatalytic activity.[37,39,40] The long-term stability of nickel silicide NiSi was investigated by galvanostatic polarization at 5 mA cm^{-2}_{disk} (**Figure 4C**). The required overpotential for NiSi decreases during the initial 4 h of operation, showing an increase in the activity. We then assign the observed electrocatalyst activation to the formation of an electrochemically active NiOOH surface layer. Later on, the activity appears to be very stable with no significant degradation for at least 17 h (the noise observed above 16 h of chronopotentiometry is attributed to unstable electrical contacts in the setup). The CVs recorded before and after 17 h chronopotentiometry (**Figure S12**) support the hypothesis of surface activation, since the reversible Ni^{3+}/Ni^{2+} redox wave experienced a large area increase.[41] The same behaviour was observed upon cycling of the o-Ni_2Si nanoparticles (**Figure S13**). The potential difference between the anodic and cathodic waves also increased, showing that the change in Ni oxidation state is slowed down after chronopotentiometry. This evolution may originate from the increased proportion of Ni^{3+} (oxy)hydroxides surface species. Despite their electrocatalytic activity, these species are electrically insulating.[38] Hence, an increase in the Ni^{3+} content should decrease the reversibility of the redox wave. The Ni $2p_{3/2}$ core level XPS spectrum of NiSi recovered after chronopotentiometry (**Figure 4D**) further corroborates the above proposed surface evolution with the emergence of a new contribution corresponding to NiOOH at a binding energy of 857 eV.[38] No Si 2p signal could be detected after chronopotentiometry (**Figure S14**), showing that surface SiO_x species were dissolved in the alkaline electrolyte and that the surface is composed mostly of a nickel oxyhydroxide-related phase. The inelastic mean free paths (IMFPs) calculated in NiOOH[42,43] were used to evaluate the depth of analysis at the Si 2p and Ni $2p_{3/2}$ energies. IMFPs are ca. 0.6 and 2 nm, respectively. Although these values should be considered with care for the analysis of powdered samples, the detection of a Ni $2p_{3/2}$ signal of Ni-Si compounds (**Figure 4D**) but the absence of the corresponding Si 2p signal (**Figure S14**) indicates that the nickel silicide phase is still present and buried below a NiOOH-like layer, which protects the Ni-Si phase from further oxidation and Si dissolution. The covalent character of the metal-metalloid bonds should impart nickel silicides with stability in

contact with the electrolyte. This could explain the small extent of oxidation, which occurs only through a thin surface layer while a conductive metal-silicon core is retained (**Figure 4D**). This remaining metallic core should enhance charge transfer through the electrode and enable faster electron transfer from the surface NiOOH electrocatalytically active species.[37,44] Such geometries, made of a layer of OER catalyst formed *in situ* and supported by a metallic, highly conductive material enhancing charge transfer have been observed on other metal-p-block element compounds,[45,46] such as metal borides,[19,39,40] metal phosphides[20,21] metal nitrides[36,37] and metal selenides.[47] The electrocatalytic activity normalized to the active catalyst mass and to the amount of nickel atoms – expected as the electrocatalytically active sites[19–21,39,40] – are comparable to, if not higher than, those reported for most nickel-p-block element electrodes processed in a similar way (**Table S3**). Thus our present work brings into light a new family of earth abundant intermetallics, namely nickel silicide nanocrystals, for electrocatalysis of the oxygen evolution reaction.

Conclusions

In conclusion, we have successfully developed a molten salts-assisted liquid-phase synthesis of nickel silicide nanocrystals with significant control of the phase purity. The surface ligand-free nanocrystals act as precatalysts that transform into OER electrocatalytically active silicides/oxide nanocomposites with high stability of their electrochemical properties under alkaline conditions. The present synthesis strategy should be effectively extended to obtain other intermetallic silicides never reported at the nanoscale to date. This perspective is currently under study. We believe that our synthesis route paves the way towards other previously inaccessible nanoscale metal silicides and towards further exploring their functional properties.

Conflicts of interest

There are no conflicts to declare.

Acknowledgements

RK acknowledges postdoctoral fellowships from the CNRS and from College de France. The authors acknowledge Madeleine Han from Lab CMCP and SOLEIL for her kind help on data conversion and Antoine Miche from Institut des Matériaux de Paris Centre for XPS measurements.

Notes and references

1 M. E. Schlesinger, *Chem. Rev.*, 1990, **90**, 607–628.
2 S. P. Murarka, *Annu. Rev. Mater. Sci.*, 1983, **13**, 117–137.
3 A. L. Schmitt, J. M. Higgins, J. R. Szczech and S. Jin, *J. Mater. Chem.*, 2010, **20**, 223–235.
4 P. Tang, Q. Zhou and S.-C. Zhang, *Phys. Rev. Lett.*, 2017, **119**, 206402.
5 P. Ritterskamp, A. Kuklya, M.-A. Wüstkamp, K. Kerpen, C. Weidenthaler and M. Demuth, *Angew. Chemie Int. Ed.*, 2007, **46**, 7770–7774.
6 R. W. Mann, L. A. Clevenger, P. D. Agnello and F. R. White, *IBM J. Res. Dev.*, 1995, **39**, 403–417.
7 M. I. Fedorov and G. N. Isachenko, *Jpn. J. Appl. Phys.*, 2015, 54.
8 X. Chen and C. Liang, *Catal. Sci. Technol.*, 2019, **9**, 4785–4820.
9 V. Johnson and W. Jeitschko, *J. Solid State Chem.*, 1972, **4**, 123–130.
10 C.-J. Kim, K. Kang, Y. S. Woo, K.-G. Ryu, H. Moon, J.-M. Kim, D.-S. Zang and M.-H. Jo, *Adv. Mater.*, 2007, **19**, 3637–3642.
11 X. Fan, H. Zhang, N. Du and D. Yang, *Mater. Res. Bull.*, 2012, **47**, 3797–3803.
12 J. M. McEnaney and R. E. Schaak, *Inorg. Chem.*, 2015, **54**, 707–709.
13 N. Dahal and V. Chikan, *Chem. Mater.*, 2010, **22**, 2892–2897.
14 M. Estruga, S. N. Girard, Q. Ding, L. Chen, X. Li and S. Jin, *Chem. Commun.*, 2014, **50**, 1454–1457.
15 Z. L. Schaefer, K. M. Weeber, R. Misra, P. Schiffer and R. E. Schaak, *Chem. Mater.*, 2011, **23**, 2475–2480.
16 S. Carenco, Z. Liu and M. Salmeron, *ChemCatChem*, 2017, **9**, 2318–2323.
17 D. Mayeri, B. L. Phillips, M. P. Augustine and S. M. Kauzlarich, *Chem. Mater.*, 2001, **13**, 765–770.
18 X. Liu, N. Fechler and M. Antonietti, *Chem. Soc. Rev.*, 2013, **42**, 8237–8265.
19 J. Masa, I. Sinev, H. Mistry, E. Ventosa, M. de la Mata, J. Arbiol, M. Muhler, B. Roldan Cuenya and W. Schuhmann, *Adv. Energy Mater.*, 2017, **7**, 1700381.
20 L. A. Stern, L. Feng, F. Song and X. Hu, *Energy Environ. Sci.*, 2015, **8**, 2347–2351.
21 J. Masa, C. Andronescu, H. Antoni, I. Sinev, S. Seisel, K. Elumeeva, S. Barwe, S. Marti-Sanchez, J. Arbiol, B. Roldan Cuenya, M. Muhler and W. Schuhmann, *ChemElectroChem*, 2019, **6**, 235–240.
22 M. S. Burke, L. J. Enman, A. S. Batchellor, S. Zou and S. W. Boettcher, *Chem. Mater.*, 2015, **27**, 7549–7558.
23 N.-T. Suen, S.-F. Hung, Q. Quan, N. Zhang, Y.-J. Xu and H. M. Chen, *Chem. Soc. Rev.*, 2017, **46**, 337–365.
24 M. Rana, S. Mondal, L. Sahoo, K. Chatterjee, P. E. Karthik and U. K. Gautam, *ACS Appl. Mater. Interfaces*, 2018, **10**, 33737–33767.
25 T. Goebel, Y. Prots and F. Haarmann, *Zeitschrift für Krist. - New Cryst. Struct.*, 2008, 223, 187.
26 M. K. Rabadanov and M. B. Ataev, *Crystallogr. Reports*, 2002, **47**, 33–38.
27 K. Toman, *Acta Crystallogr.*, 1952, **5**, 329–331.
28 A. Franciosi, J. H. Weaver and F. A. Schmidt, *Phys. Rev. B* , 1982, **26**, 546–553.
29 W. Hume-Rothery and G. V Raynor, *The Structure of Metals and A lloys*, The Institute of Metals, London, 1956.
30 P. T. Andrews, T. Collins and P. Weightman, *J. Phys. C Solid State Phys.*, 1981, **14**, L957–L960.
31 P. J. Grunthaner, F. J. Grunthaner and J. W. Mayer, *J. Vac. Sci. Technol.*, 1980, **17**, 924–929.
32 P. Lorenz, J. Finster, G. Wendt, J. V Salyn, E. K. Žumadilov and V. I. Nefedov, *J. Electron Spectros. Relat. Phenomena*, 1979, **16**, 267–276.
33 A. N. Mansour, *Surf. Sci. Spectra*, 1994, **3**, 231–238.
34 R. B. Shalvoy, P. J. Reucroft and B. H. Davis, *J. Catal.*, 1979, **56**, 336–348.
35 K. S. W. Sing, D. H. Everrtt, R. A. W. Haul, L. Moscou, R. A. Pierotti, J. Rouquerol and T. Siemieniewska, *Pure Appl. Chem.*,

1985, **57**, 603–619.
36 K. Xu, P. Chen, X. Li, Y. Tong, H. Ding, X. Wu, W. Chu, Z. Peng, C. Wu and Y. Xie, *J. Am. Chem. Soc.*, 2015, **137**, 4119–4125.
37 M. Shalom, D. Ressnig, X. Yang, G. Clavel, T. P. Fellinger and M. Antonietti, *J. Mater. Chem. A*, 2015, **3**, 8171–8177.
38 N. Weidler, J. Schuch, F. Knaus, P. Stenner, S. Hoch, A. Maljusch, R. Schäfer, B. Kaiser and W. Jaegermann, *J. Phys. Chem. C*, 2017, **121**, 6455–6463.
39 J. Masa, P. Weide, D. Peeters, I. Sinev, W. Xia, Z. Sun, C. Somsen, M. Muhler and W. Schuhmann, *Adv. Energy Mater.*, 2016, **6**, 1502313.
40 H. Li, P. Wen, Q. Li, C. Dun, J. Xing, C. Lu, S. Adhikari, L. Jiang, D. L. Carroll and S. M. Geyer, *Adv. Energy Mater.*, 2017, **1700513**, 1700513.
41 P. Wilde, S. Dieckhöfer, T. Quast, W. Xiang, A. Bhatt, Y.-T. Chen, S. Seisel, S. Barwe, C. Andronescu, T. Li, W. Schuhmann and J. Masa, *ACS Appl. Energy Mater.*, 2020, **3**, 2304–2309.
42 NIST Electron Inelastic Mean Free Path Database (Version 1.2) ©2010, U.S. Secretary of Commerce.
43 S. Tanuma, C. J. Powell and D. R. Penn, *Surf. Interface Anal.*, 1991, **17**, 911–926.
44 R. Nesper, *Angew. Chemie Int. Ed. English*, 1991, **30**, 789–817.
45 S. Jin, *ACS Energy Lett.*, 2017, **2**, 1937–1938.
46 B. R. Wygant, K. Kawashima and C. B. Mullins, *ACS Energy Lett.*, 2018, **3**, 2956–2966.
47 S. Kim, H. Mizuno, M. Saruyama, M. Sakamoto, M. Haruta, H. Kurata, T. Yamada, K. Domen and T. Teranishi, *Chem. Sci.*, 2020, **11**, 1523–1530.